*robotics*

MDPI

*Article*

# Navigating ALICE: Advancements in Deployable Docking and Precision Detection for AUV Operations

**Yevgeni Gutnik [1,*], Nir Zagdanski [1], Sharon Farber [1], Tali Treibitz [1] and Morel Groper [2]**

[1] The Hatter Department of Marine Technologies, Leon H. Charney School of Marine Sciences, University of Haifa, Haifa 3498838, Israel; nzagdansk@univ.haifa.ac.il (N.Z.); sharonf@alumni.technion.ac.il (S.F.); ttreibitz@univ.haifa.ac.il (T.T.)

[2] Faculty of Mechanical Engineering, Technion, Israel Institute of Technology, Haifa 3200003, Israel; morelg@technion.ac.il

* Correspondence: ygutnik@campus.haifa.ac.il

**Abstract:** Autonomous Underwater Vehicles (AUVs) operate independently using onboard batteries and data storage, necessitating periodic recovery for battery recharging and data transfer. Traditional surface-based launch and recovery (L&R) operations pose significant risks to personnel and equipment, particularly in adverse weather conditions. Subsurface docking stations provide a safer alternative but often involve complex fixed installations and costly acoustic positioning systems. This work introduces a comprehensive docking solution featuring the following two key innovations: (1) a novel deployable docking station (DDS) designed for rapid deployment from vessels of opportunity, operating without active acoustic transmitters; and (2) an innovative sensor fusion approach that combines the AUV's onboard forward-looking sonar and camera data. The DDS comprises a semi-submersible protective frame and a subsurface, heave-compensated docking component equipped with backlit visual markers, an electromagnetic (EM) beacon, and an EM lifting device. This adaptable design is suitable for temporary installations and in acoustically sensitive or covert operations. The positioning and guidance system employs a multi-sensor approach, integrating range and azimuth data from the sonar with elevation data from the vision camera to achieve precise 3D positioning and robust navigation in varying underwater conditions. This paper details the design considerations and integration of the AUV system and the docking station, highlighting their innovative features. The proposed method was validated through software-in-the-loop simulations, controlled seawater pool experiments, and preliminary open-sea trials, including several docking attempts. While further sea trials are planned, current results demonstrate the potential of this solution to enhance AUV operational capabilities in challenging underwater environments while reducing deployment complexity and operational costs.

**Keywords:** launch and recovery system (LARS); autonomous underwater vehicle (AUV); sensor fusion; forward-looking sonar (FLS); AUV docking



Academic Editor: David Portugal

Received: 30 November 2024
Revised: 25 December 2024
Accepted: 30 December 2024
Published: 31 December 2024

**Citation:** Gutnik, Y.; Zagdanski, N.; Farber, S.; Treibitz, T.; Groper, M. Navigating ALICE: Advancements in Deployable Docking and Precision Detection for AUV Operations. *Robotics* **2025**, *14*, 5. https://doi.org/10.3390/robotics14010005



## 1. Introduction

Autonomous underwater vehicles (AUVs) are unmanned and untethered robots capable of operating autonomously for extended periods without the need for manned supervision or surface support. These capabilities make them suitable for various tasks, including seabed survey and monitoring [1–3], inspection of offshore structures [4], mine countermeasures [5], and intervention [6]. Nevertheless, while untethered operation grants AUVs the freedom to cover extensive areas without the need for tether management, it also

constrains their operational endurance to the capacity of onboard batteries, which becomes particularly critical during surface operations requiring continuous thrust to maintain position, as well as in data collection tasks, which are constrained to the opportunities for transferring the collected data.

Traditionally, to recharge batteries and exchange data, AUVs are required to surface and be manually recovered to a support the surface vessel using the vessel's onboard crane or another dedicated lifting mechanism. On the surface, most AUVs face significant operational constraints due to their limited energy reserves for opposing waves and currents, combined with environmental disturbances affecting their attitude control [7,8]. As a result, autonomous or remote control of the AUV on the surface is limited, necessitating manual recovery from the vessel for most recovery operations. Furthermore, the relative motion between the AUV and the vessel, especially in adverse weather conditions and rough seas, makes surface launch and recovery (L&R) challenging and dangerous for the involved personnel and equipment.

Specialized docking stations (DS), designed for underwater docking, have the potential to reduce the complexity and risks associated with surface L&R operations. Fixed on the seabed and located close to offshore infrastructure, subsurface DSs can support continuous operation without the need for periodic surface recovery [9]. This concept has been extensively studied, leading to the proposal of various designs. Directional docking within a protective frame or funnel [10–15] allows the protection of the AUV from the environment and eases the connection interface with the dock. However, this method requires the precise alignment between the AUV and the dock. This constraint may be challenging, particularly in scenarios where side currents cause the AUV to drift. To reduce the necessity for alignment, a concept of docking with a pole or wire was developed and is used mainly in automated launch and recovery systems (LARS) [16–19].

Integrating LARS with a subsurface docking component allows the critical docking phase to occur below the surface, protecting the AUV from surface waves and wind effects. However, this setup often requires the AUV to carry a specialized line capture device, potentially limiting payload capacity and impacting hydrodynamic performance. Additionally, while submerged, communication with the AUV is limited, so detection and guidance to the dock must be performed autonomously by the AUV, relying on onboard acoustic sensors, vision cameras, electromagnetic (EM) sensing, or a combination of these technologies [9].

Acoustic systems, such as ultra-short baseline systems (USBL) and compatible transponder are commonly employed for docking guidance due to their relatively extensive detection range [20]. However, when these sensors are used, the AUV must be rigged with a receiver and the docking station with a transponder. Furthermore, their limited data rate (approximately 1 Hz) makes them unsuitable for the terminal docking guidance phase. Consequently, studies such as [21–23] have proposed combining USBL systems with high-speed vision cameras to improve docking guidance, where the USBL facilitates far-field guidance and the camera is used during the terminal guidance phase.

Electromagnetic (EM)-based guidance relies mainly on the measurements of artificially generated magnetic fields to estimate the distance and pose with respect to the dock [24–28]. Electromagnetic fields remain unaffected by water conditions and do not require a direct line of sight. Nevertheless, due to the attenuation of the EM field, its applicability may be limited to the terminal guidance phase.

Vision cameras provide the benefit of high-resolution and high-speed data acquisition (approximately 5–10 Hz). Additionally, they provide both azimuth and elevation data, making them valuable for docking guidance [23]. However, they require an uninterrupted line of sight and are sensitive to environmental factors such as water turbidity and lighting.

Moreover, monocular cameras are often inadequate for the complete pose estimation, requiring the integration of light arrays in known configurations [16,29,30] or the use of fiducial markers [31] on the dock.

Forward-looking sonars (FLS) can provide distance and direction information within ranges of approximately 100 m. Unlike vision cameras, FLS data remain unaffected by visibility conditions. Furthermore, unlike other acoustic sensors, such as USBL, these sensors offer high-resolution data at a relatively high rate. FLS data, however, are usually represented as synthetic images, providing only two-dimensional information, range and azimuth. Moreover, the detection of objects is highly dependent on their acoustic reflectance. Consequently, FLS sensors are primarily used for mapping and obstacle avoidance [32,33], but they are seldom utilized for docking guidance [34,35].

Given that FLSs provide distance and vision cameras that offer elevation data, their fusion may complement each other [36]. This concept has been widely explored for enhancing object detection and 3D reconstruction [37,38] or to improve simultaneous localization and mapping (SLAM) algorithms [39]. Although this approach may provide a precise position and facilitate docking guidance, the integration of FLS and FLC for underwater docking is rarely used [40] and has not yet been sufficiently researched and validated for optimal implementation.

This study addresses these challenges by introducing a comprehensive solution that integrates novel hardware and software approaches. As illustrated in Figure 1, we present a first-of-its-kind deployable docking system (DDS) specifically designed for subsurface, omnidirectional docking and the recovery of small-sized AUVs from a "vessel of opportunity". Our approach advances the state-of-the-art model through two fundamental innovations: First, unlike conventional systems that rely on acoustic beacons, our DDS operates entirely without transmitting components—a significant advancement that enables operations in acoustically sensitive areas. Second, we introduce a novel multi-sensor fusion approach that leverages the AUV's existing onboard forward-looking sonar (FLS) and forward-looking camera (FLC) for guidance, achieving precise and reliable 3D positioning without additional specialized equipment. The system has been successfully integrated and tested with the ALICE AUV [1], and its scalable design enables its adaptation to other AUVs equipped with similar sensor configurations.

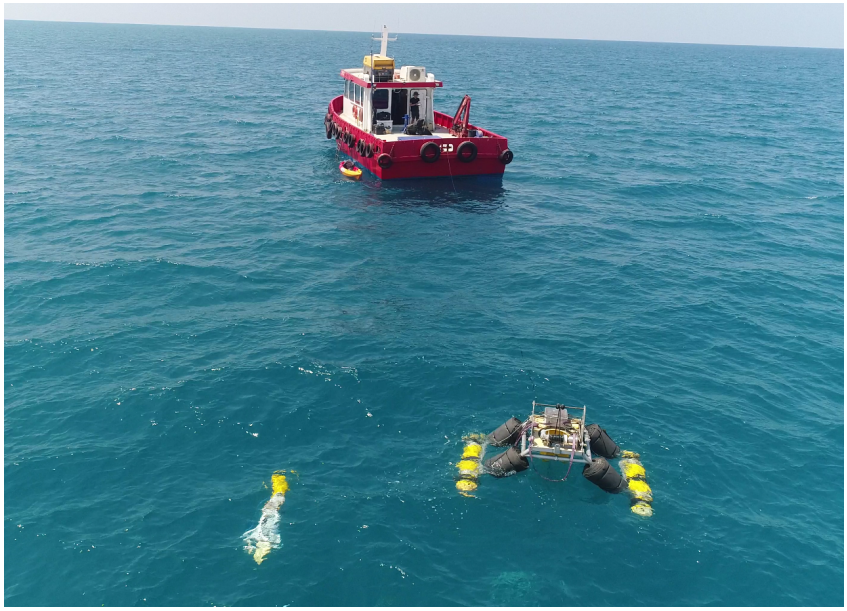

**Figure 1.** The DDS and ALICE AUV deployed from a small vessel during an experiment at sea.

The sections of this paper are structured as follows. Section 2 provides a comprehensive overview of the developed DDS and the docking AUV. Section 3 outlines the developed dock detection and positioning method. Section 4 describes the docking sequence and the various guidance phases. System validation through simulation, pool experiments, and a preliminary experiment at sea are presented in Section 5, and the results are discussed in Section 6. Finally, Section 7 summarizes the findings and presents our concluding remarks.

## 2. System Description

### *2.1. DDS*

The DDS was designed as a self-powered deployable system capable of effectively launching and recovering small AUVs under challenging sea conditions. To facilitate subsurface docking, the system consists of a floating platform and a subsurface docking component, as depicted in Figures 2 and 3 and detailed in Table 1.

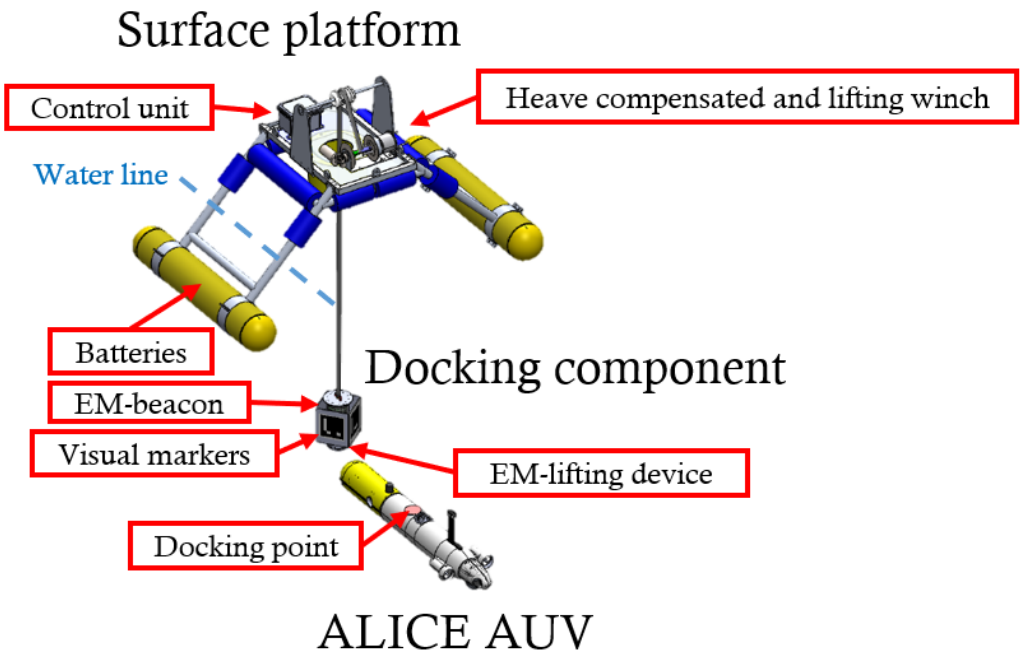


**Figure 2.** An overview on the DDS components.

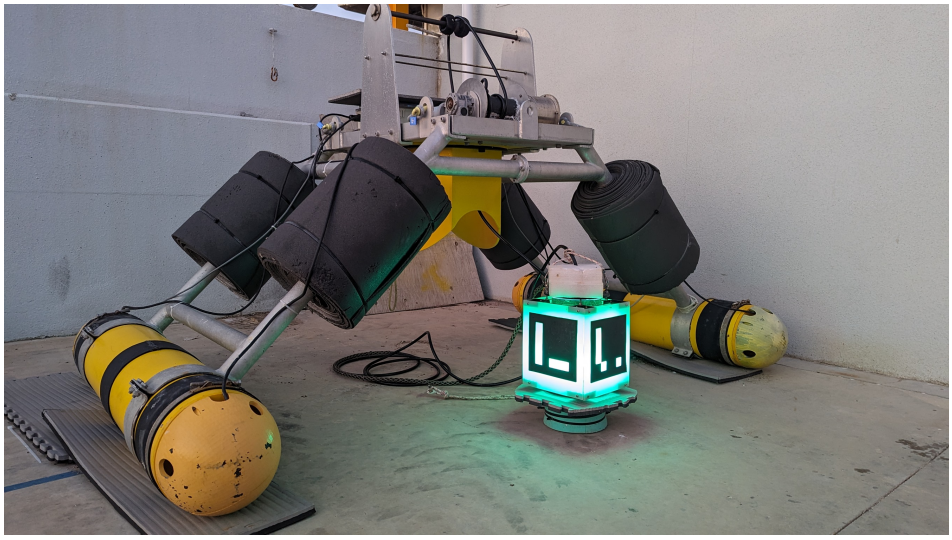

**Figure 3.** DDS surface platform and docking component.

**Table 1.** DDS main components.

| DDS | |
|---|---|
| Dimensions (L × W × H) | 1.4 m × 2.6 m × 1.48 m |
| Weight | 250 kg |
| Controller | SparkFun Thing Plus ESP32 |
| Communication | WiFi/433 Mhz (on/off switch) |
| Winch | EZ Anchor Puller Hero EX-1 |
| Slip ring | CENO electronics 16 pin, IP67 |
| Power | 12V 4 × 25 Ah lead–acid battery |
| Pressure sensor | Blue Robotics Bar02 ultra-high resolution |

#### 2.1.1. Docking Component (Figure 4)

The subsurface docking component is equipped with the essential elements that support the guidance and latching of the AUV. It consists of an acrylic, optically clear watertight enclosure, 6 inches in diameter, in which guiding LEDs, an EM beacon, and a high-resolution pressure sensor were integrated. To enhance internal heat dissipation, the enclosure is filled with 3M™ Novec™ 7100 engineered fluid. Four backlit-illuminated fiducial ArUco markers [41] were installed around the enclosure to enable pose estimation, regardless of the direction of the AUV approach. The black patterns of these markers were 3D-printed and attached to white, semi-transparent ABS plates to diffuse the LED lights and facilitate the uniform illumination of the markers. This concept not only extends their detection range but also provides a visual beacon for longer distances.

A 24 V lifting electromagnet, capable of lifting 60 kg, was attached to the bottom of the enclosure to latch the AUV from its center of gravity. Power and communication to the component were supplied from the surface platform through an 18-pin SubConn bulkhead connector and a cable 10 m in length, which also doubles as the cable for lifting the AUV to the surface platform. To relieve tension from the connector, a fleeter, commonly known as "Chinese fingers", was attached to the cable and connected to slings located on the aluminum end-cup of the housing. The weight of the docking component ensures that the lifting line remains stable and under tension, while a heave compensation controller maintains the system at a constant depth.

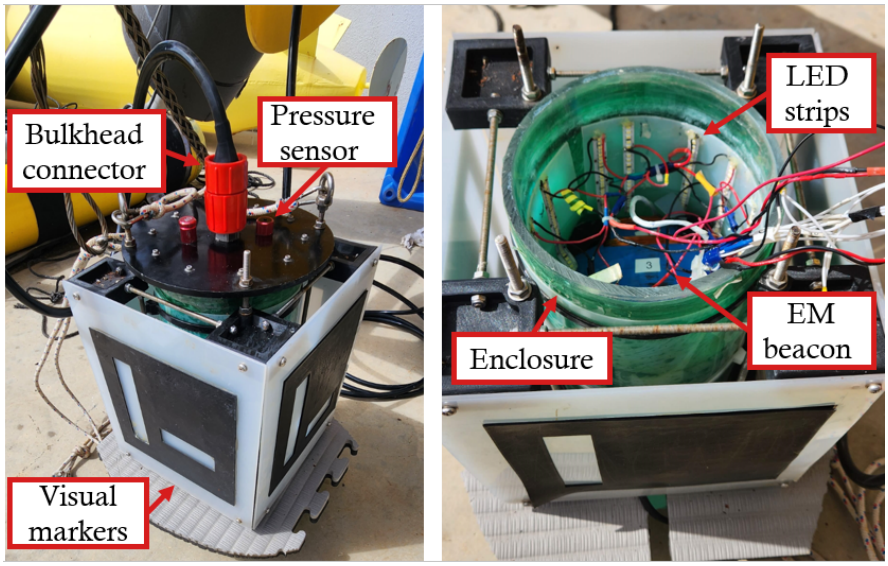


**Figure 4.** Components of the subsurface docking component.

2.1.2. Surface Platform (Figure 5)

The surface platform is designed as a semi-submersible structure and serves a dual purpose, protecting the AUV during transfer to/from the support vessel and enhancing stability by minimizing wave impact in challenging sea conditions. The platform is constructed with an aluminum frame for structural integrity. Two positively buoyant cylindrical floaters, manufactured from ABS plastic and attached to the frame, provide buoyancy while housing the batteries and water leak detection sensors. A self-alignment mechanism placed between the floaters guides the AUV to maintain proper alignment during the lifting process. The spacing between the floats was specifically designed to enable the smooth lifting of the ALICE AUV into the self-aligning component. The dimensions of the floats, along with additional foam attached to the DDS frame, were carefully chosen to achieve the desired draft, reducing the impact of waves while maintaining the surface platform's top relatively dry and ensuring hydrostatic stability.

A mechanical winch mounted on the platform controls the depth of the docking component during operations and retrieves the AUV to a protected position between the floaters. During standby mode, while awaiting AUV docking, the winch maintains a constant depth and compensates for the platform's heave motion through a dedicated heave compensation controller using feedback from a pressure sensor mounted on the docking component. The winch control functions are implemented on an ESP-32 microcontroller. A 433-MHz remote switch serves both as a system activator and as a safety kill switch. The docking component is equipped with a water-resistant enclosure housing the microcontroller, the remote switch relay, a power distribution board, voltage converters, and power amplifiers for the EM beacon. A slip-ring mechanism on the winch allows data and power transfer to the subsurface docking component. I2C communication between the ESP32 and the pressure sensor is enabled through two PCA9615 differential transceivers, extending communication over the 10-m cable and slip ring. External communication with the microcontroller is facilitated via the ESP WiFi module, allowing the remote configuration of the depth of the docking component, the activation of the EM beacon, and the monitoring of the leak sensors.

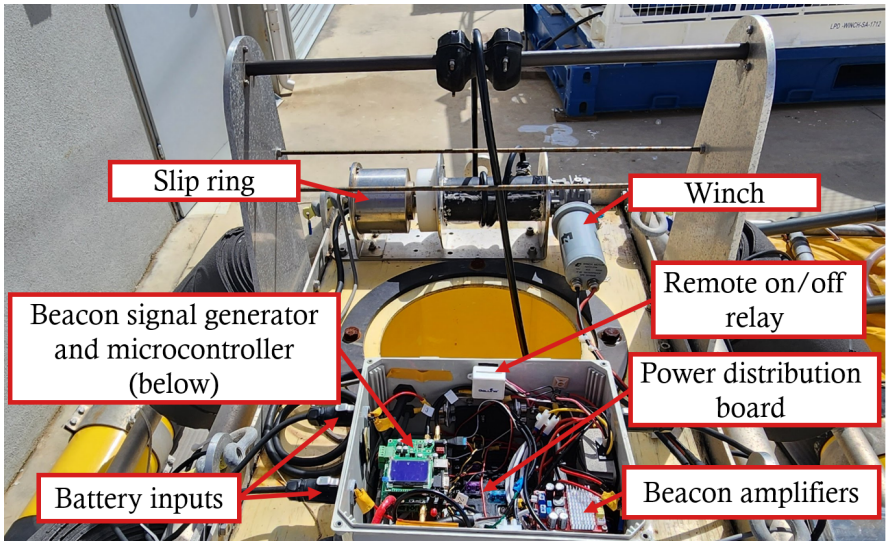


**Figure 5.** The surface platform components.

## 2.2. ALICE

ALICE [1] is a modified version of the IQUA Robotics SPARUS II AUV [42]. This AUV, characterized by its compact and lightweight design, can operate at speeds up to 3 knots and depths of up to 200 m. The AUV's propulsion system relies on five thrusters that facilitate its

hovering capability and precise, decoupled yaw motion control. Specifically, two horizontal thrusters control the surge and yaw, two lateral thrusters control the sway and yaw, and a single vertical thruster controls the heave motion. Notably, roll and pitch motions are not actively controlled. For underwater navigation, ALICE is equipped with an inertial navigation system (INS), a pressure sensor, and an acoustic Doppler velocity log (DVL). These sensors are integrated with an extended Kalman filter (EKF) to provide navigation and pose solutions. When the AUV is on the sea surface, the system corrects drift over time using a global positioning system (GPS) module located inside its mast. Optionally, when submerged, the position can be corrected by a USBL system. The latter method, however, requires the deployment of a transmitter from the support vessel. Importantly, for the presented DDS, USBL was not used as project requirements specifically prohibited active acoustic transmissions from the docking station. ALICE's control and communication architecture is based on an open source software framework named COLA2, implemented within the robotic operating system (ROS) environment [43]. The current configuration of ALICE employed in this study, as detailed in Table 2, was equipped with a Teledyne BlueView M900 FLS and an Allied Vision Manta-G917 FLC. The latter was installed in a specially in-house designed, compact, water-resistant enclosure featuring a 4-inch dome port to minimize optical distortions. The FLS and FLC sensors were installed in the front payload section, as shown in Figures 6 and 7. The FLS was operated through an ABS-made cover to preserve the AUV's hydrodynamic design. To latch the lifting electromagnet of the docking component, a metal attachment plate was installed on top of the AUV's hull, near its center of gravity.

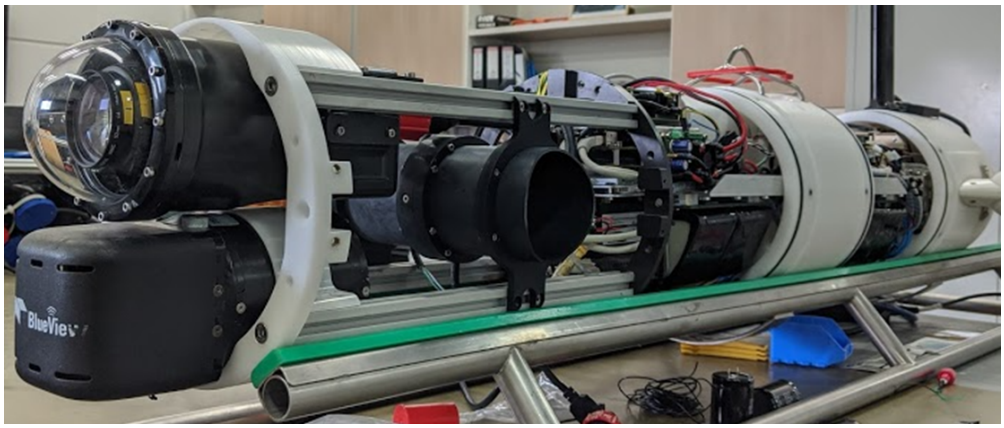

**Figure 6.** ALICE AUV (disassembled) with FLS and FLC in the front payload section.

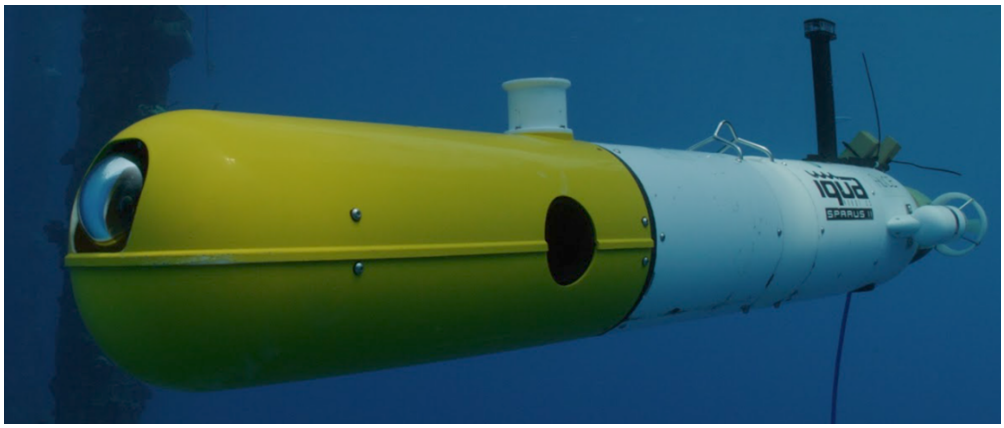

**Figure 7.** ALICE during experiment at sea.

**Table 2.** ALICE AUV specifications.

| **ALICE—A Modified SPARUS II AUV** | |
|---|---|
| General dimensions | |
| Length | 2 m |
| Hull diameter | 230 mm |
| Max width | 0.46 m |
| Weight in air | 60 kg |
| Performance | |
| Maximal depth | 200 m |
| Max surge velocity | 3 knots |
| Endurance | 8–10 h |
| Battery | 1.9 kWh |
| Propulsion system | 5 thrusters |
| Controllable DoFs | Surge, sway, yaw, heave |
| Navigation system | |
| DVL | Teledyne RDI Explorer 600 |
| IMU | ADIS16488, MEMS, 6°/h in-run bias |
| Pressure sensor | Keller PA-9LD, 30 bar, 0.15%FS accuracy |
| GPS | Fastrax IT500 |
| Docking and obstacle avoidance sensors | |
| Forward-looking sonar | Teledyne BlueView M900 |
| Forward-looking camera | Allied Vision Manta-G917 9.2 MP |
| Software | Open source—ROS Melodic over Linux Ubuntu 18.04 |

## 3. Detection and Positioning of the DDS

The detection and positioning of the DDS was performed by employing the on-board FLS, FLC, and magnetometers. To optimize detection accuracy, these sensors were utilized in three distinct phases of guidance, as illustrated in Figure 8. In the far-field phase, positioning was performed only by the FLS, which was expected to detect the DDS from a distance of circa 50 m. The FLS, however, is capable of providing only the horizontal position of the DDS and was unable to provide the depth of the docking component.

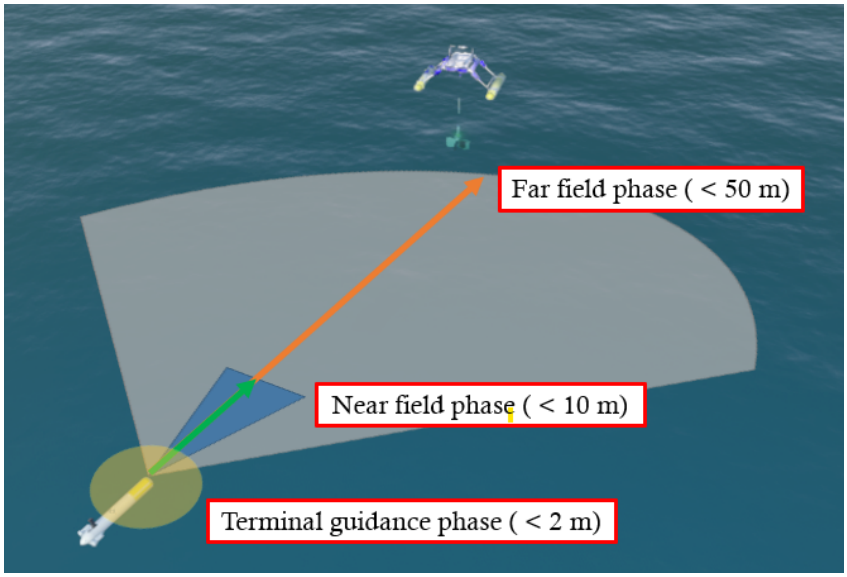


**Figure 8.** Three guidance phases of the docking sequence, defined by the detection range and field of view of the FLS, FLC, and the magnetometers.

During the near-field phase, the FLC and FLS data are fused to provide an accurate 3D position of the subsurface docking component. This phase is initiated as the DDS enters the FLC's detection range, estimated at around 10 m from the docking component.

In the terminal guidance phase, the AUV utilizes its onboard magnetometers to determine the position of a beacon installed on the docking component. This phase begins when ALICE is within approximately 2 m of the docking component, at which distance the AUV's magnetometer can detect the EM beacon.

This paper focuses on the novel positioning method developed for the near-field guidance phase, while the terminal guidance phase using electromagnetic sensing is detailed in [28].

### *3.1. FLS Image Processing*

The FLS is a multibeam sonar system that transmits acoustic pulses and calculates the range and azimuth by measuring the time of flight of the reflections received by each transducer. This process generates a 2D image in which each pixel represents the intensity of the received reflections, while the pixel indices correspond to the range and azimuth of the reflection. The acoustic reflections from a spatial point $P_s$ are typically processed by the FLS in spherical coordinates consisting of range $(r)$, azimuth $(\theta_s)$, and elevation $(\phi_s)$, defined as follows:

$$P_s = \begin{bmatrix} x_s \\ y_s \\ z_s \end{bmatrix} = \begin{bmatrix} r\cos\theta_s\cos\phi_s \\ r\sin\theta_s\cos\phi_s \\ r\sin\phi_s \end{bmatrix} \tag{1}$$

Due to its operational principle, the FLS cannot distinguish between reflections from the same range and azimuth at different elevations. As a result, these reflections are mapped to the same point on the FLS image. The mapping of the point $P_s$ onto the FLS image frame, represented by $P'_s$ with $u_s$ and $v_s$ denoting the indices of the corresponding pixel, as illustrated in Figure 9, is given as follows:

$$P'_s = \begin{bmatrix} u_s \\ v_s \end{bmatrix} = \begin{bmatrix} r\cos\theta_s \\ r\sin\theta_S \end{bmatrix} = \frac{1}{\alpha \cdot \cos\phi_s} \begin{bmatrix} x_s \\ y_s \end{bmatrix} \tag{2}$$

In this context, $\alpha\left[\frac{\text{m}}{\text{pixel}}\right]$ represents the sonar resolution. Given that the vertical field of view angle is 20°, the maximum angle to be considered for projection into the sonar image plane is ±10°. Accordingly, the small angle approximation can be employed to define $\cos\phi_s \approx 1$.

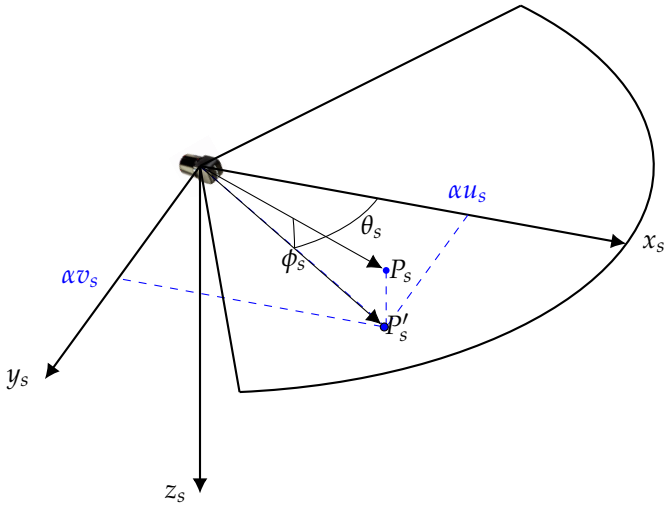


**Figure 9.** FLS coordinate frame.

FLS data often consist of noise attributed to factors such as acoustic reverberations, signal scattering, variations in sensitivity between FLS transducers [32], interference originating from AUV's electronics, and other acoustic sensors such as DVL [33]. Noises associated with varying transducer sensitivities result in artifacts at constant azimuth, as illustrated in Figure 10a. To eliminate these artifacts, the Hough line transform was applied to adaptively mask the noise that appears at constant azimuth. This process is illustrated in Figure 10b, where straight black lines at constant azimuths mask the artifacts (represented by gray lines) that exceed a certain threshold. Sparse electronic noise, characterized by momentary high-intensity artifacts, was suppressed by averaging every two consecutive frames (denoted $I_1$ and $I_2$) as follows:

$$I_{\mathrm{d}} = \frac{I_1(u_s, v_s) + I_2(u'_s, v'_s)}{2} \tag{3}$$

The pixels in $I_2$ are displaced to compensate for the AUV's motion between the frames after the following transformation:

$$\begin{bmatrix} u'_s \\ v'_s \end{bmatrix} = \mathbf{R}_i^s \begin{bmatrix} u_s \\ v_s \end{bmatrix} + \frac{1}{\alpha} \begin{bmatrix} \Delta x_0 \\ \Delta y_0 \end{bmatrix} \tag{4}$$

where $[\Delta x_0, \Delta y_0]^T$ represents the linear displacements and $\mathbf{R}_i^s$ the angular displacement, as computed by the AUV's navigation filter. The remaining noise was reduced by applying a median blurring filter [44]. The outcome of applying the averaging and the median filter is illustrated in Figure 10c.

An adaptive threshold was computed for each frame to distinguish objects from the background. This threshold was set by analyzing the peaks in the image histogram, with pixels that exceeded the threshold intensity classified as objects, as demonstrated in the resulting binary image in Figure 10d.

The DDS was identified by searching for the object that matches its physical dimensions. To improve robustness in cases where only parts of the DDS were detected as objects, smaller elements were clustered based on a distance threshold corresponding to the dimensions of the DDS, using hierarchical agglomerative clustering [45].

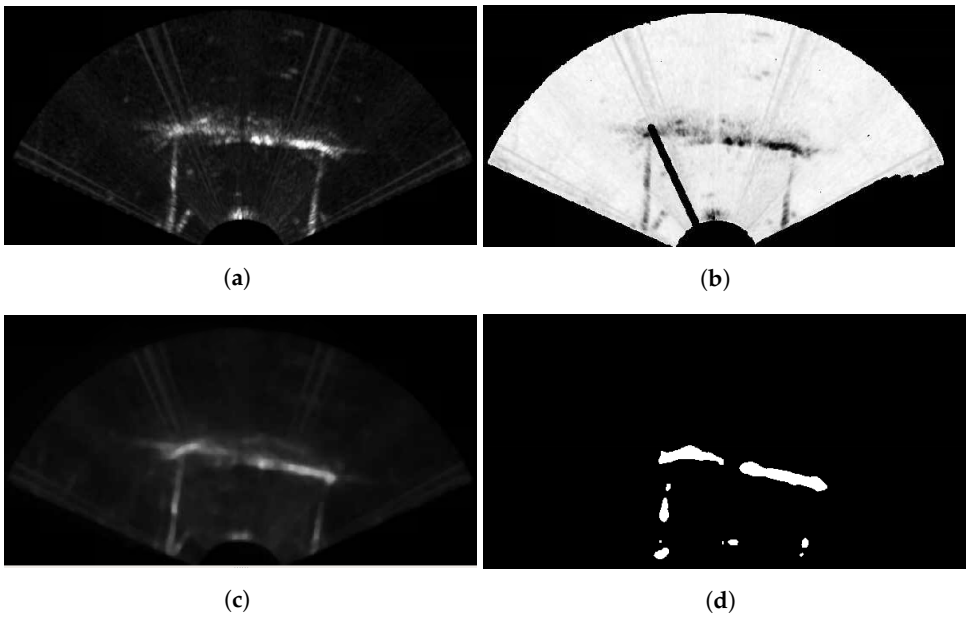

(**a**) (**b**)

(**c**) (**d**)

**Figure 10.** (**a**) The FLS data in the seawater pool experiment; (**b**) adaptive beam mask; (**c**) two-frame averaged and median blur image; and (**d**) thresholded binary image.

### *3.2. FLC Detection*

The vision-based detection involves two main processes as follows: First, the LEDs on the docking component are detected, enabling the computation of its horizontal and vertical directions. Second, the ArUco marker [46] patterns are used to calculate its 3D position, as illustrated in Figure 11. This combined approach enhances detection, as the LED illumination extends the detectable range of the docking component, while the markers provide precise positioning at distances up to approximately 3 m.

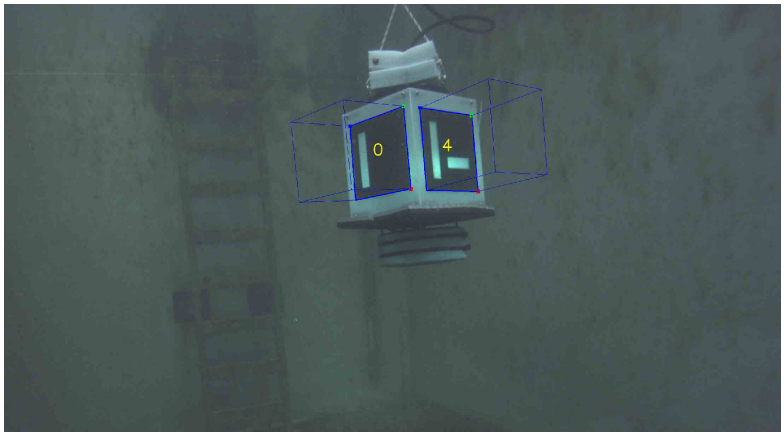


**Figure 11.** The ArUco markers, as detected by the ArUco detection algorithm.

The detection of the LEDs in the FLC image relies on identifying clusters of pixels with specific parameters of HSV (hue, saturation, value) [47], which were determined through simulations and pool experiments, as illustrated in Figure 12.

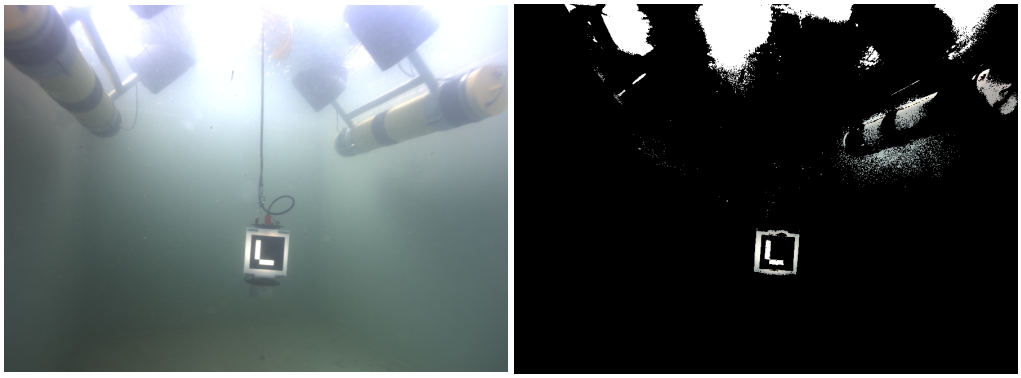

(**a**) (**b**)

**Figure 12.** (**a**) The DDS as detected by the FLC in the pool experiment. (**b**) Extracted objects using the HSV threshold.

The transformation of a point from the FLC's Cartesian frame $[x_c, y_c, z_c]^T$ to its image frame $[u_c, v_c]^T$ is defined by the pinhole camera model [48] as follows:

$$\begin{bmatrix} u_c \\ v_c \\ 1 \end{bmatrix} = \begin{bmatrix} f_x & 0 & c_x \\ 0 & f_y & c_y \\ 0 & 0 & 1 \end{bmatrix} \begin{bmatrix} x_c \\ y_c \\ z_c \end{bmatrix} \frac{1}{z_c} \tag{5}$$

where $f_x$ and $f_y$ represent the focal lengths and $c_x$, $c_y$ denote the offsets between the FLC's optical center and the origin of the image's pixel coordinates, as illustrated in Figure 13.

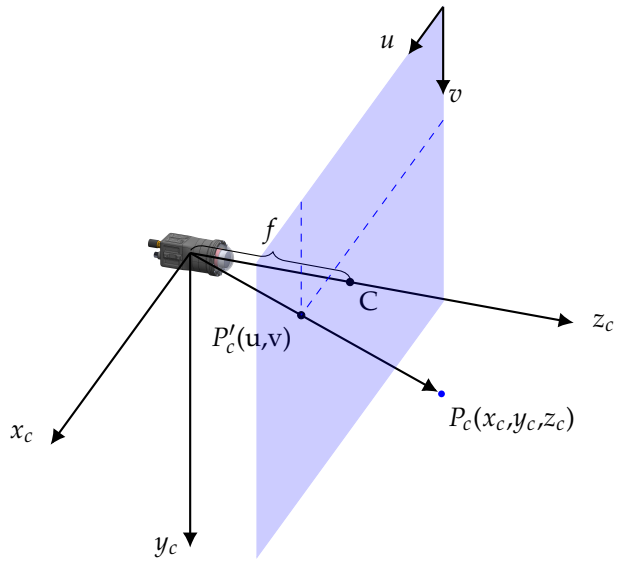


**Figure 13.** FLC's coordinate frame.

The focal length and offset are intrinsic parameters of the FLC, obtained by calibration. Using this projection, the azimuth ($\theta_c$) and elevation ($\phi_c$) angles are computed as follows:

$$\begin{aligned} \theta_c &= \tan^{-1}\left(\frac{x_c}{z_c}\right) = \tan^{-1}\left(\frac{u_c - c_x}{f_x}\right) \\ \phi_c &= \tan^{-1}\left(\frac{y_c}{z_c}\right) = \tan^{-1}\left(\frac{v_c - c_y}{f_y}\right) \end{aligned} \tag{6}$$

From Equation (5) it is evident that the 3D position of the docking component can only be determined if the distance $z_c$ is known. Therefore, in this phase, the FLS data were used in combination with the LED detection process.

### *3.3. FLS-FLC Fusion*

The fusion between FLC and FLS leverages the ALICE on-board sensor configuration, as depicted in Figure 6 and illustrated in Figure 14. Here, $z_c$ can be determined from the range information provided by the FLS. To incorporate this information, the FLS data was transformed into the FLC frame through the transformation $T_s^c = [\mathbf{R}_s^c \quad \mathbf{t}_s^c]$, where $\mathbf{R}_s^c$ is a rotation matrix defined by the rotation angles between the FLS and FLC frames $(\psi_s^c, \theta_s^c, \phi_s^c)$, which represent the rotations about the $x_s$, $y_s$, and $z_s$ axes, respectively:

$$\mathbf{R}_\mathbf{s}^\mathbf{c} = \begin{pmatrix} \mathrm{c}\psi\mathrm{c}\phi & \mathrm{s}\theta\mathrm{s}\psi\mathrm{c}\phi - \mathrm{c}\theta\mathrm{s}\phi & \mathrm{c}\theta\mathrm{s}\psi\mathrm{c}\phi + \mathrm{s}\theta\mathrm{s}\phi \\ \mathrm{c}\psi\mathrm{s}\phi & \mathrm{s}\theta\mathrm{s}\psi\mathrm{s}\phi + \mathrm{c}\theta\mathrm{c}\phi & \mathrm{c}\theta\mathrm{s}\psi\mathrm{s}\phi - \mathrm{s}\theta\mathrm{c}\phi \\ -\mathrm{s}\psi & \mathrm{s}\theta\mathrm{c}\psi & \mathrm{s}\theta\mathrm{c}\psi \end{pmatrix} \tag{7}$$

where c denotes the cos and s the sin functions. In addition, $\mathbf{t}_s^c$ defines the linear displacement of the FLC frame with respect to the FLS frame as follows

$$\mathbf{t}_s^c = [x_s^c, y_s^c, z_s^c]^T \tag{8}$$

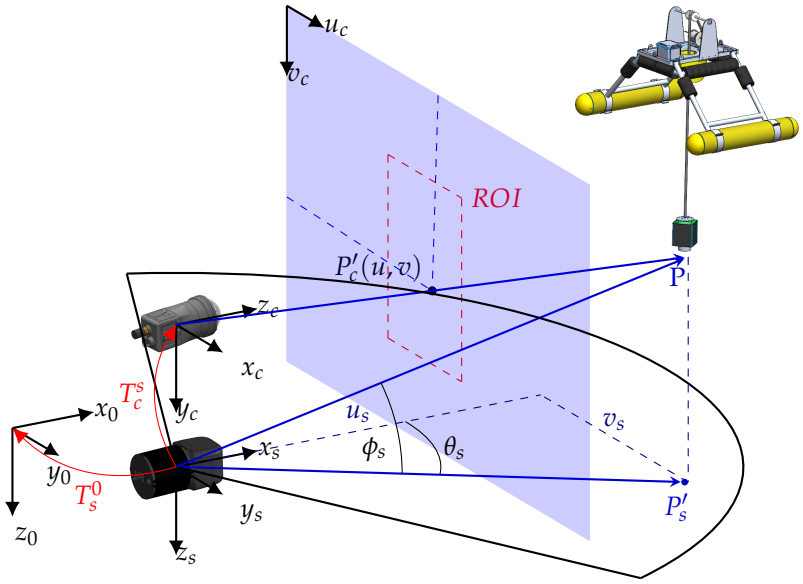


**Figure 14.** FLC and FLS coordinate frames.

The values of $\mathbf{R}_s^c$ and $\mathbf{t}_s^c$ can be obtained through extrinsic calibration methods [49,50] or by assuming the precise installation of the sensors and measuring from the AUV's CAD model, as employed in this study. Consequently, the transformation between $P_s$ and $P_c$ is defined as follows:

$$P_c = \mathbf{R}_s^c P_s + t_s^c \tag{9}$$

By employing the small-angle approximation on the FLS' elevation angle $\cos\phi_s \approx 1$ and substituting Equation (1) into Equation (9) we obtain the following:

$$\begin{bmatrix} x_c \\ y_c \\ z_c \end{bmatrix} = \mathbf{R}_s^c \begin{bmatrix} r\cos\theta_s \\ r\sin\theta_s \\ \phi_s \end{bmatrix} + t_s^c \tag{10}$$

Considering the current sensor configuration and neglecting installation errors, the rotation between the FLS and FLC frames is defined by the angles $\phi_s^c = -\frac{\pi}{2}$, $\theta_s^c = 0$, $\psi_s^c = -\frac{\pi}{2}$. Consequently, the rotation matrix $\mathbf{R}_s^c$ is given as follows:

$$\mathbf{R}_s^c = \begin{pmatrix} 0 & 1 & 0 \\ 0 & 0 & 1 \\ 1 & 0 & 0 \end{pmatrix} \tag{11}$$

and $z_c$ is expressed by the following:

$$z_c = r\cos\theta_s + x_s^c \tag{12}$$

By substituting Equation (12) into Equation (6), the position of the docking component with respect to the FLC frame is given by the following:

$$\begin{aligned} x_c &= \frac{u_c - c_x}{f_x}(r\cos\theta_s + x_s^c) \\ y_c &= \frac{v_c - c_y}{f_y}(r\cos\theta_s + x_s^c) \\ z_c &= r\cos\theta_s + x_s^c \end{aligned} \tag{13}$$

where the condition $\theta_c = \theta_s$ was used to match the objects detected by the FLS and those the FLC.

To enhance FLC detection, the range and azimuth to the DDS, obtained from the FLS, were combined with data from the depth sensor and predefined parameters for the docking component's deployment depth to establish a region of interest (ROI) on the FLC image. The ROI was used to confine the search for the LED light within a specified sector of the image. This enhances the robustness of the detection algorithm by disregarding reflections and other false detections outside the ROI. Likewise, it improves computational efficiency.

The horizontal bounds of the ROI in the FLC image frame, denoted by $\{u_c^{min}, u_c^{max}\}$, were determined by enforcing the registration condition $\theta_c = \theta_s$ on Equation (6) and introducing the offset parameter $w$ to establish the width of the ROI window as follows:

$$\begin{aligned} u_c^{min} &= \frac{f_x(x_c + w)}{z_c} + c_x \\ u_c^{max} &= \frac{f_x(x_c - w)}{z_c} + c_x \end{aligned} \tag{14}$$

The vertical bounds of the ROI, represented by $\{v_c^{min}, v_c^{max}\}$, were determined using Equation (6) and by incorporating physical constraints to determine $\{y_c^{min}, y_c^{max}\}$. Considering that the FLS cannot detect objects located outside its field of view, denoted by $\theta_s^{max}$, and above the sea surface, and taking into account that the docking component is deployed within the depth limits $\{d^{min}, d^{max}\}$, the vertical bounds of the ROI were defined as follows:

$$\begin{aligned} v_c^{min} &= \frac{f_y y_c^{min}}{z_c} + c_y \\ v_c^{max} &= \frac{f_y y_c^{max}}{z_c} + c_y \end{aligned} \tag{15}$$

where

$$\begin{aligned} y_c^{min} &= max\{-Z, -r\sin\theta_s^{max}\} \\ y_c^{max} &= min\{max\{0, d^{max} - Z\}, r\sin\theta_s^{max}\} \end{aligned} \tag{16}$$

Here, $Z$ represents the depth of the AUV, as measured by the onboard pressure sensor.

## 4. Docking Sequence

The three-phase docking sequence utilizes the position information obtained from the FLS, FLC, and magnetometers to guide the AUV to the docking position. Each phase involves sending a specific set of position and heading demands to the AUV's control system. The sequence begins by directing the AUV towards the "last known" position of the DDS at a predetermined depth, anticipating the detection of the DDS by the FLS during this maneuver. Upon detection, the far-field guidance phase is initiated. Throughout this phase, the position of the DDS is computed by the FLS where the depth is predefined.

Near-field guidance begins when the FLC detects the docking component. In this phase, the three-dimensional guidance relies on the FLS-FLC fusion and, subsequently, on ArUco markers. Upon detecting an ArUco marker, the AUV's holonomic motion controller [1] is activated to precisely guide the AUV to the "handshake" position. At this point, the position of the docking component, calculated using the ArUco markers, initializes the EM-based positioning algorithm. During terminal guidance, this EM-based algorithm guides the AUV beneath the docking component until it securely attaches to the lifting electromagnet.

The docking sequence was implemented onboard the AUV using the ROS SMACH state machine library, designed for building hierarchical state machines. A simplified version of the docking sequence created with SMACH is shown in Figure 15. The docking sequence began with the "go-to" command (denoted EXECUTE_GOTO_MISSION in the SMACH framework), which provided a 3D goal point for the AUV. Simultaneously, the FLS detection node actively searched for the DDS. Upon detection by the FLS, the FLS-based guidance (FLS_DETECT) was activated. The transition from the far-field to the near-field phase occurred either upon detecting the illumination of the docking component (BULB_DETECT) or upon recognizing the markers (ARUCO_DETECT).

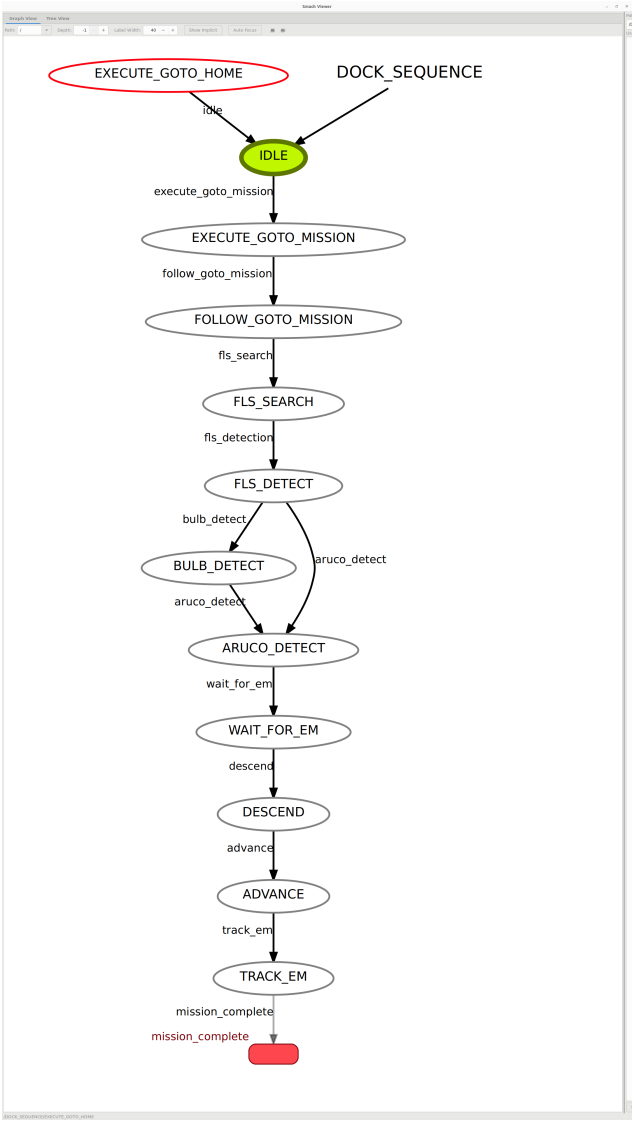


**Figure 15.** The docking sequence as displayed by the SMACH viewer.

The terminal guidance phase was initiated with the detection of the EM beacon and the initialization of the EM-based positioning algorithm, as detailed in [28]. To avoid potential collisions between the docking component and the AUV's hull or appendages, this phase was divided into four maneuvering states. First, the AUV descended to a depth of 0.5 m below the docking component (DESCEND). At this depth, it advanced beneath the docking component (ADVANCE) to minimize the distance between the onboard magnetometer and the beacon, thereby improving electromagnetic field detection.

Subsequently, the AUV utilized EM-based guidance (TRACK_EM) to accurately position itself below the docking component while maintaining a consistent depth. Upon

reaching the target position within a 15 cm tolerance, the final state (MISSION_COMPLETE) was activated. In this state, the vertical thruster was deactivated, allowing the AUV's positive buoyancy to lift it gently until it securely attached to the lifting electromagnet. It is worth noting that at this stage of development, failed attempts were not handled automatically. Instead, manual intervention was required to return to the previous state, using the last known position of each state as a reference point.

## 5. System Validation

### *5.1. Simulation*

The developed docking system was initially evaluated using the StoneFish simulation tool [51]. This simulation combines a physics engine, sensor plugins, a rendering pipeline to provide a realistic 3D virtual world and interface to ALICE's control and navigation architecture, along with dedicated sensor plugins to simulate FLS and FLC data. Therefore, it was utilized for software-in-the-loop testing of the developed algorithms within the AUV's control architecture.

To simulate docking scenarios, the DDS was incorporated as a static model, with the surface platform fixed to the sea surface and the subsurface docking component submerged to a depth of 2.5 m. The LED light on the docking component was represented by an omnidirectional bulb. Additionally, a static model of a small support vessel was introduced to simulate a realistic scenario, as depicted in Figure 16a. Importantly, the simulated FLS images synthesized the DDS and support vessel based on their physical CAD models, while acoustic reflections and multipath problems were not modeled. Therefore, simulated FLS images were mainly used for the initial evaluation of the FLS-based detection algorithm, as shown in Figure 16b, and for testing the FLS-FLC fusion algorithm, as illustrated by the computed ROI around the docking component in Figure 16c.

(**a**)

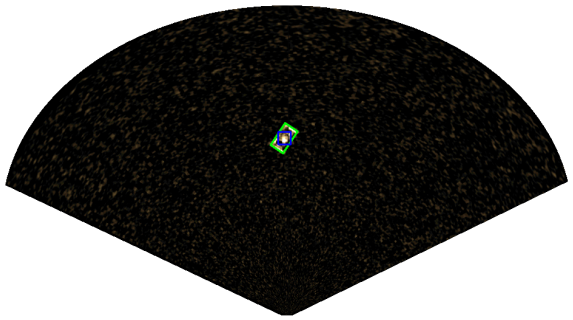

(**b**)

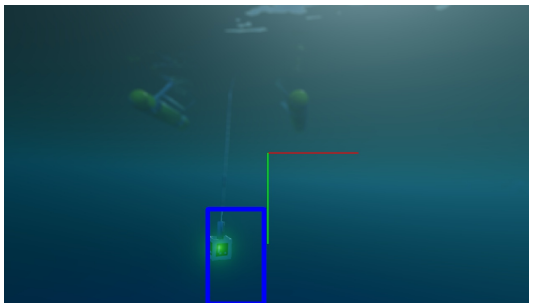

(**c**)

**Figure 16.** (**a**) Stonefish scene features the ALICE AUV, DDS, and a support vessel. (**b**) The processed FLS image with the green rectangle representing the detected DDS and the blue rectangle signifying the tracked entity. (**c**) Simulated FLC image with the ROI (represented by blue rectangle) defined according to the detection of the DDS in the FLS image. The green and red lines signifying the coordinate frame of the FLC image.

To test the docking sequence, a model of ALICE was positioned 50 m in front of the DDS and directed toward its approach position at a depth of 3 m. Once the FLS detected the docking component, the docking sequence wes automatically activated, guiding ALICE at a constant depth until the LEDs were detected by the FLC. At this point, the FLS-FLC fusion algorithm calculated the 3D position of the component, guiding ALICE to this position until the ArUco markers were detected. After detection, ALICE was guided to the "handshake" position. Finally, the terminal guidance phase was simulated using the last known position of the docking component. The trajectory of ALICE and the positioning results computed by the guidance algorithms are shown in Figure 17.

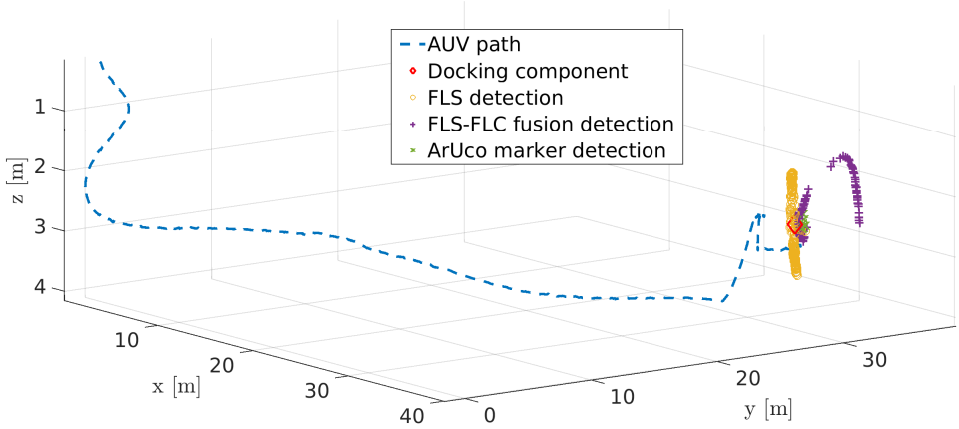


**Figure 17.** ALICE's path and the positioning of the docking component as computed by the FLS and FLC detection and fusion algorithms in the Stonefish simulation

### *5.2. Pool Experiments*

Following the simulation evaluation, the algorithms were tested in an outdoor seawater pool (9 m × 3 m × 2.8 m − L × W × H), as illustrated in Figure 18. The natural light conditions and seawater environment enabled the assessment and fine-tuning of the algorithms' parameters under varying visibility and illumination conditions. During these experiments, the DDS was deployed with its docking component submerged at approximately 1.5 m depth. To evaluate the detection and positioning algorithms, ALICE was maneuvered at various distances from the docking component while recording data from all sensors.

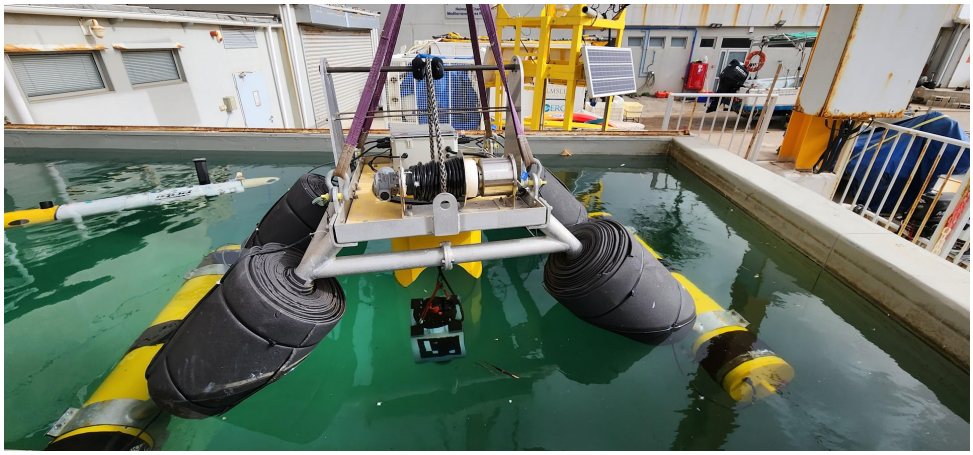

**Figure 18.** DDS and ALICE in a pool experiment.

The confined dimensions of the pool posed challenges for the detection of the surface platform by the FLS, as the acoustic signature of the platform was difficult to distinguish from the pool walls. Therefore, the pool tests focused primarily on the following two aspects: detecting the docking component (as illustrated in Figure 19) and evaluating ALICE's precise motion control while approaching and maintaining the "handshake" position. The positioning results from different detection algorithms are presented in Figure 20. The experiments revealed that the uneven LED illumination of the markers adversely affected their detection accuracy. This issue was addressed by reducing the intensity of the LEDs and adding diffusing material between the LEDs and markers. Additionally, to improve the FLC processing rate, the camera resolution was reduced to 136 by 196 pixels.

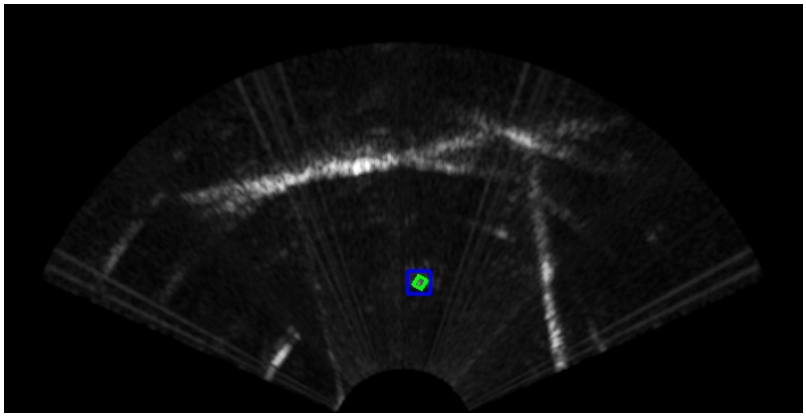

(**a**)

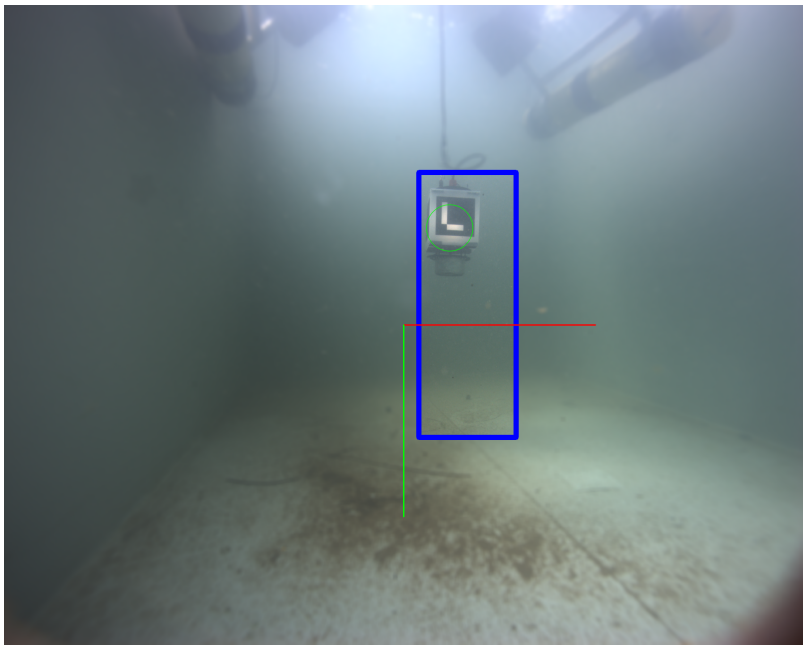

(**b**)

**Figure 19.** (**a**) The docking component as obtained by the FLS, set to the maximal range of 6 m, with the green rectangle representing the detected object and the blue rectangle indicating the most probable docking component entity. (**b**) The docking component as obtained by the FLC, with the blue rectangle representing the ROI defined by the fusion algorithm and the green cycle indicating the HSV-based detection of the docking component. The red and green lines represent the axes of the image frame.

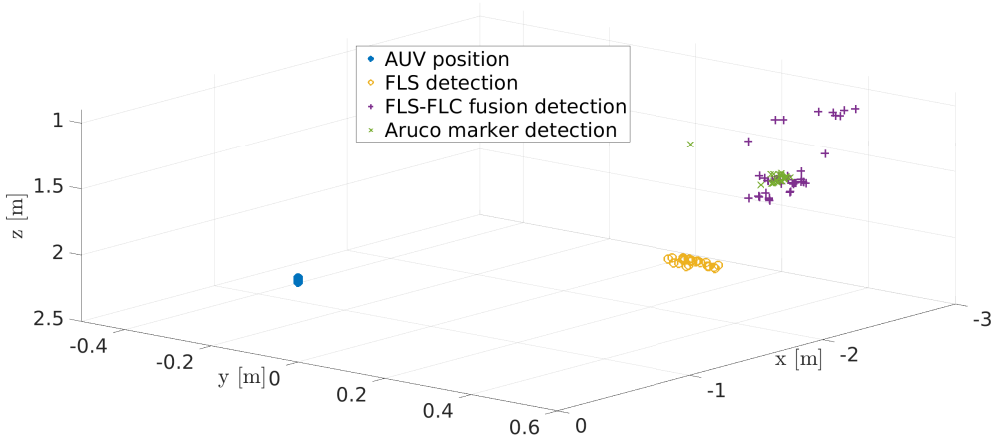


**Figure 20.** The positioning of the DDS' docking component as computed by the FLS, the FLS-FLC fusion, and the ArUco marker detection algorithms.

### *5.3. Preliminary Sea Trial*

As a crucial step towards real-world validation, a preliminary sea trial was conducted in the Haifa Bay area. The primary objectives of this test were to assess the basic stability and dynamics of the DDS under actual sea conditions and to perform an initial evaluation of the detection algorithms in a real sea environment. During the trial, the DDS was deployed from a support vessel (Figure 21a) while the docking component was set at a depth of 4.5 m. After deployment, ALICE was submerged to a depth of 3 m and manually controlled at various distances in front of the DDS, as illustrated in Figure 21b. Despite challenging conditions, including extremely noisy FLS data, these tests yielded encouraging results. The DDS was detected from a distance of 25 m, as shown in Figure 22, and provided an ROI window within the FLC image, as illustrated in Figure 23a. The detection of the guiding LEDs, however, revealed areas for improvement. The illumination of the LEDs proved inadequate for consistent detection at the planned ranges. Instead, the system detected the white buoy atop the docking component from a distance of 4 m. As ALICE ventured closer, the ArUco markers were successfully detected 2.5 m from the component, as shown in Figure 23b.

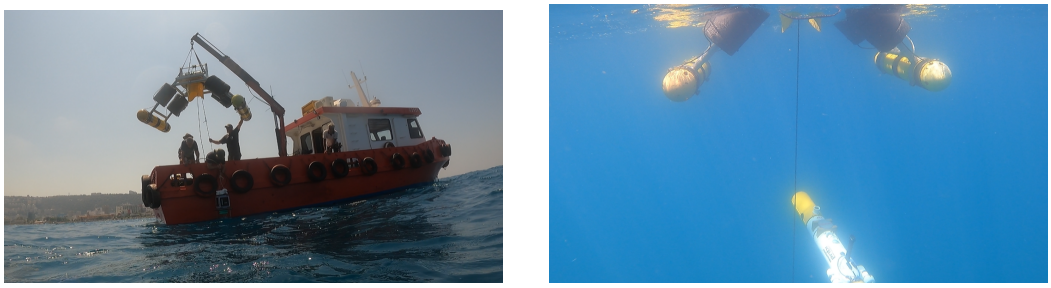

(**a**) (**b**)

**Figure 21.** (**a**) DDS deployment from a support vessel at sea. (**b**) ALICE AUV and the DDS during the experiment at sea.

Finally, two autonomous docking attempts were made. During the first attempt, ALICE was remotely guided toward the general vicinity of the DDS at a depth of 3 m, with the maximum FLS range set to 18 m. The detection and guidance algorithms were performed as designed, with the docking component successfully detected within the FLC's ROI from a distance of 4 m, prompting the appropriate depth adjustment commands. While using a basic experimental speed controller (which will be replaced in future work with advanced control algorithms) at a 0.5 m/s surge speed, the AUV made contact with the

docking component (Figure 23c). The second attempt focused on validating the closed-field guidance capabilities. ALICE was manually positioned 3.5 m from the DDS at a depth of 2.5 m, where the FLS detected the DDS as expected. The autonomous sequence was executed according to the design, again demonstrating effective sensor fusion and guidance performance, although the experimental speed controller again resulted in contact with the docking component. The final phase trajectory of the first attempt, recorded by the navigation system, along with the goal positions determined by the detection algorithms and the position of the docking component (identified by the AUV's location at contact), is depicted in Figure 24. These results validate the primary objectives of the experiment, that is that the detection algorithms performed with the expected accuracy, successfully guiding ALICE to the docking component position. The contact incidents were attributable to the simplified experimental controller, which will be replaced with a dedicated docking controller in future work focusing on terminal guidance and control.

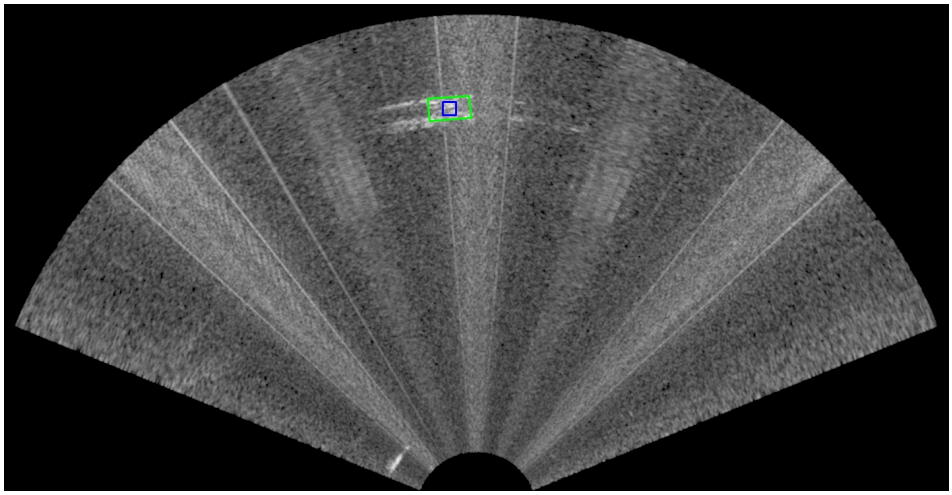

**Figure 22.** The FLS image, configured at its maximum range of 25 m, captures the DDS' surface platform as observed at sea. The green rectangle represents the detected object and the blue rectangle indicates the tracked entity.

Consequently, although the first trial was limited in scope and duration, it provided invaluable insights into the system's performance in real marine conditions. The successful long-range detection via FLS and short-range detection via FLC demonstrate the potential of our multi-sensor approach.

(**a**) (**b**) (**c**)

**Figure 23.** Results of the experiment at sea: (**a**) The detection of the docking component, indicated by rec cycle within the ROI. (**b**) The detection of the ArUco markers. (**c**) Collusion with the docking component.

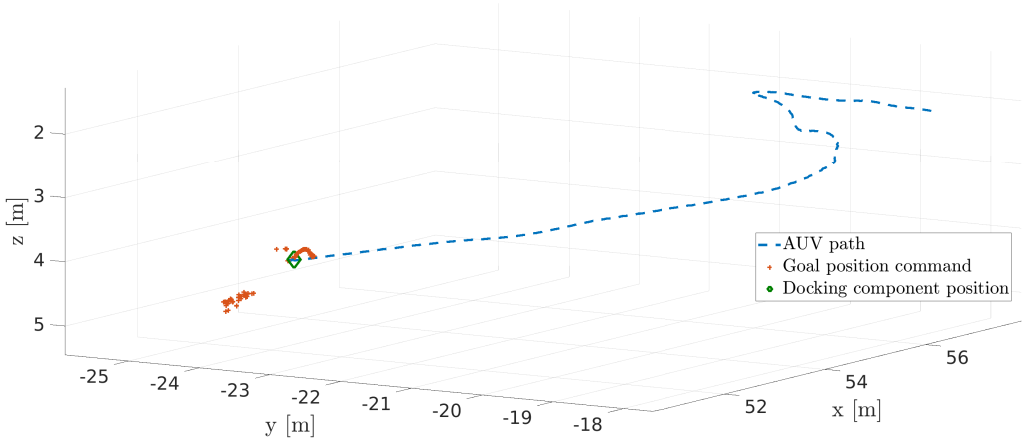


**Figure 24.** ALICE's trajectory, the docking component's position, and the goal points as recorded during the first sea docking attempt.

In addition, the data collected during the experiment were used for the further adjustments of the FLC's detection algorithm, in particular, a rectification of the upper and lower bounds of the ROI based on the depth of the DDS and an increase in the resolution of the processed FLC image to 3384 by 2710 pixels. As a result of these optimizations, the FLC-based detection of the docking component was extended to 5.5 m, and false detections were effectively excluded. The results of the adjusted detection algorithm, applied to the recorded data, are illustrated in Figure 25. These challenges will be taken into account and attempts will be made to resolve them in future sea experiments. The detection ranges during the pool and sea experiments are summarized in Table 3.

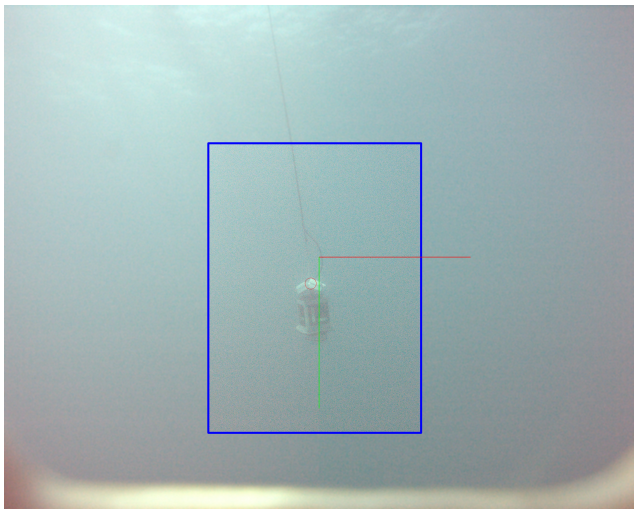

**Figure 25.** The detection of the docking component by the HSV filter, marked by the red circle, and the ROI, marked by the blue rectangle.

**Table 3.** Detection performance in pool and sea experiments.

| Location | AUV Depth [m] | Dock Depth [m] | FLS Detection Range [m] | FLC Detection Range (Light) [m] | FLC Detection Range (ArUco) [m] |
|---|---|---|---|---|---|
| Pool | 2 | 1.5 | 8 | 4 | 3 |
| Sea (actual) | 3 | 4.5 | 25 | 4 | 2.5 |
| Sea (after enhancement) | 3 | 4.5 | 25 | 5.5 | 2.5 |

## 6. Discussion

The results of the experiments conducted in both the pool and at sea demonstrated the potential of the developed DDS system and the FLS-FLC fusion-based docking guidance to enable the subsurface docking and recovery of AUVs using small vessels and without the need for active acoustic beacons on the docking system. This beacon-free deployable approach marks a significant advance in AUV docking technology, especially for applications in noise-sensitive areas or for covert operations. Specifically, the tests confirmed the following:

- The successful deployment of the DDS confirmed its practical applicability in real-world scenarios.
- The FLS-FLC fusion, tested primarily in pool experiments, demonstrated its ability to provide 3D positioning. The precision of the fusion was verified by comparing the 3D positions calculated by the fusion algorithm with those obtained using the ArUco marker pose estimation algorithm. As shown in Figure 20, the computed positions exhibited an accuracy of less than 10 cm in most cases, with deviations mainly caused by false detections of one or both sensors. It is worth noting that the accuracy of the ArUco algorithm had previously been validated by positioning ALICE at fixed distances from the markers and comparing the calculated distances with actual measurements.
- The FLS-FLC fusion-based ROI concept effectively eliminated false detections and improved the computational efficiency of vision-based detection. Its effectiveness was demonstrated in the experiments, where, without restricting the detection to a specific region, ambient light from the surface and reflections from the DDS floaters were often detected together with the docking component, as shown by the white regions in Figure 12b. These false detections were successfully eliminated by applying the ROI and incorporating deployment constraints. This allowed accurate detection even under challenging conditions, where the docking component and the surface exhibited similar HSV values, as demonstrated in Figure 19b.
- The experiments highlighted the effectiveness of backlit illumination for ArUco markers, significantly increasing their detection range and providing an innovative solution to improve their detection under low-visibility conditions. This finding also suggests that this setup could be adapted for a wide range of robotic applications that utilize similar markers for positioning and control under low-visibility conditions.

While these results are promising, the experiments also identified several challenges that require further investigation and refinement as follows:

- Although the FLS image denoising algorithm demonstrated its effectiveness during pool and sea trials, Figure 10d indicates that certain parts of the object, such as the pool walls, did not exceed the adaptive threshold. This highlights the need for the further optimization of the adaptive threshold to improve performance. Furthermore, noise associated with varying transducer sensitivities was found to increase significantly in longer ranges, likely due to higher gain settings. This is evident when comparing Figures 19a and 22, which were configured for the maximum ranges of 6 m and 25 m, respectively. These results suggest that integrating the FLS maximum range parameter into the algorithm could enable the dynamic adjustment of the noise threshold values, enhancing its adaptability and accuracy.
- The FLS data consisted of a significant level of noise, even at close ranges of 25 m in calm sea conditions with relatively clear water, as presented in Figure 22. This finding suggests that either the FLS parameters need further adjustment or there may be

strong electrical interference. Future work will focus on optimizing FLS performance in various sea conditions.

- While most of the experiments were conducted while the AUV was submerged to 3 m and the docking component was set to 4.5 m, further experiments are needed to identify the optimal AUV depth and FLS settings to increase the detection range of the DDS. This optimization process will be crucial for enhancing the system's effectiveness in diverse underwater environments.
- The FLS-based detection of the DDS is not fully robust in scenarios where nearby objects have physical characteristics similar to those of the DDS. To improve reliability, we plan to train a neural network on the collected FLS data for the detection of the DDS.
- Under open sea conditions in daylight, the illumination of the LEDs was inadequate for robust vision-based detection, as presented in Figure 23b. To satisfy the detection range while maintaining the uniform illumination of the markers, further adjustments to the light intensity as well as the selection of a better wavelength and better deployment depth will be performed.
- Considering the enhanced performance achieved with high-resolution data processing, as shown in Table 3, the FLC image processing algorithm will be further optimized for real-time performance by implementing it on the AUV's Jetson AGX Orin GPU. This hardware optimization is expected to significantly enhance the system's operational efficiency.
- The approach speed during terminal guidance was found to be too high. To enhance the robustness of the approach, the surge speed during close-field guidance will be limited to 0.1 m/s.

Although significant, these challenges provide clear directions for future research and development. Our future work will focus on addressing these issues through a combination of hardware improvements, algorithm refinements, and extensive sea trials.

## 7. Conclusions

This work has introduced an innovative approach for the underwater docking and recovery of AUVs through two major contributions. First, we developed a novel deployable docking station (DDS) that uniquely combines rapid deployment capability with beacon-free operation. The system's ability to operate without acoustic transmitters represents a significant advancement, particularly for operations in acoustically sensitive environments or during covert missions. Second, we demonstrated a robust sensor fusion approach that leverages existing AUV sensors (forward-looking sonar and camera) for precise 3D positioning, eliminating the need for external acoustic positioning systems. The effectiveness of these innovations was systematically validated through the following:

- Comprehensive software-in-the-loop simulations demonstrating the viability of the sensor fusion concept.
- Controlled seawater pool experiments verifying the precision of the detection and positioning algorithms.
- Preliminary sea trials confirming the system's deployability and basic functionality in real marine conditions.

Although our preliminary sea trials identified areas that require further refinement, particularly in LED illumination intensity and approach speed control, they also confirmed the fundamental soundness of our approach. Future work will focus on the following:

- Optimizing FLS performance and detection algorithms for varying sea conditions.
- Enhancing vision-based detection range and reliability.

- Implementing speed control refinements for terminal approach.
- Conducting comprehensive sea trials in diverse environmental conditions.

The successful demonstration of this integrated docking solution, combining novel hardware design with innovative sensor fusion, represents a significant step toward more flexible and cost-effective AUV operations. By eliminating the need for permanent installations and expensive acoustic positioning systems while maintaining robust performance, this approach opens new possibilities for AUV operations in both scientific research and industrial applications.

**Author Contributions:** Conceptualization, Y.G., S.F. and M.G.; methodology, Y.G., S.F., T.T. and M.G.; software, Y.G. and N.Z.; validation, Y.G. and N.Z.; formal analysis, Y.G.; investigation, Y.G.; resources, M.G. and T.T.; data curation, Y.G., N.Z. and T.T.; writing—original draft preparation, Y.G. and M.G.; writing—review and editing, M.G. and T.T.; visualization, Y.G. and N.Z.; supervision, M.G.; funding acquisition, M.G. and T.T.; All authors have read and agreed to the published version of the manuscript.

**Funding:** This research was funded by the Leona M. and Harry B. Helmsley Charitable Trust and The Maurice Hatter Foundation.

**Data Availability Statement:** The data presented in this study are available on request from the corresponding author.

**Acknowledgments:** The authors would like to thank Uri Katz, Amir Dayan, and Uri Graiver.

**Conflicts of Interest:** The authors declare no conflicts of interest.

## Abbreviations

The following abbreviations are used in this manuscript:

| | |
|---|---|
| AUV | Autonomous underwater vehicle |
| L&R | Launch and recovery |
| DDS | Deployable docking station |
| DS | Docking station |
| FLS | Forward-ooking sonar |
| FLC | Forward-ooking camera |
| USBL | Ultra-short baseline |
| DVL | Doppler velocity log |

## References

1. Gutnik, Y.; Avni, A.; Treibitz, T.; Groper, M. On the adaptation of an auv into a dedicated platform for close range imaging survey missions. *J. Mar. Sci. Eng.* **2022**, *10*, 974. [CrossRef]
2. Pizarro, O.; Friedman, A.; Bryson, M.; Williams, S.B.; Madin, J. A simple, fast, and repeatable survey method for underwater visual 3D benthic mapping and monitoring. *Ecol. Evol.* **2017**, *7*, 1770–1782. [CrossRef] [PubMed]
3. Carballini, J.; Viana, F. Using synthetic aperture sonar as an effective tool for pipeline inspection survey projects. In Proceedings of the 2015 IEEE/OES Acoustics in Underwater Geosciences Symposium (RIO Acoustics), Rio de Janeiro, Brazil, 29–31 July 2015; pp. 1–5.
4. Albiez, J.; Joyeux, S.; Gaudig, C.; Hilljegerdes, J.; Kroffke, S.; Schoo, C.; Arnold, S.; Mimoso, G.; Alcantara, P.; Saback, R.; et al. Flatfish-a compact subsea-resident inspection auv. In Proceedings of the OCEANS 2015-MTS/IEEE Washington, Washington, DC, USA, 19–22 October 2015; pp. 1–8.
5. Palomeras, N.; Furfaro, T.; Williams, D.P.; Carreras, M.; Dugelay, S. Automatic target recognition for mine countermeasure missions using forward-looking sonar data. *IEEE J. Ocean. Eng.* **2021**, *47*, 141–161. [CrossRef]
6. Ridao, P.; Carreras, M.; Ribas, D.; Sanz, P.J.; Oliver, G. Intervention AUVs: The next challenge. *Annu. Rev. Control* **2015**, *40*, 227–241. [CrossRef]
7. Li, D.; Du, L. Auv trajectory tracking models and control strategies: A review. *J. Mar. Sci. Eng.* **2021**, *9*, 1020. [CrossRef]

8. Tian, W.; Song, B.; Ding, H. Numerical research on the influence of surface waves on the hydrodynamic performance of an AUV. *Ocean Eng.* **2019**, *183*, 40–56. [CrossRef]
9. Yazdani, A.M.; Sammut, K.; Yakimenko, O.; Lammas, A. A survey of underwater docking guidance systems. *Robot. Auton. Syst.* **2020**, *124*, 103382. [CrossRef]
10. Hurtós, N.; Mallios, A.; Palomeras, N.; Bosch, J.; Vallicrosa, G.; Vidal, E.; Ribas, D.; Gracias, N.; Carreras, M.; Ridao, P. LOON-DOCK: AUV homing and docking for high-bandwidth data transmission. In Proceedings of the OCEANS 2017-Aberdeen, Aberdeen, UK, 19–22 June 2017; pp. 1–7.
11. Hobson, B.W.; McEwen, R.S.; Erickson, J.; Hoover, T.; McBride, L.; Shane, F.; Bellingham, J.G. The development and ocean testing of an AUV docking station for a 21" AUV. In Proceedings of the OCEANS 2007, Aberdeen, UK, 18–21 June 2007; pp. 1–6.
12. Gu, H.t.; Meng, L.; Bai, G.; Zhang, H.; Lin, Y.; Liu, S. Automated recovery of the UUV based on the towed system by the USV. In Proceedings of the 2018 OCEANS-MTS/IEEE Kobe Techno-Oceans (OTO), Kobe, Japan, 28–31 May 2018; pp. 1–7.
13. Jalving, B.; Faugstadmo, J.E.; Vestgard, K.; Hegrenaes, O.; Engelhardtsen, O.; Hyland, B. Payload sensors, navigation and risk reduction for AUV under ice surveys. In Proceedings of the OCEANS 2008, Quebec City, QC, Canada, 15–18 September 2008; pp. 1–8.
14. Lin, M.; Lin, R.; Yang, C.; Li, D.; Zhang, Z.; Zhao, Y.; Ding, W. Docking to an underwater suspended charging station: Systematic design and experimental tests. *Ocean Eng.* **2022**, *249*, 110766. [CrossRef]
15. Page, B.R.; Mahmoudian, N. AUV docking and recovery with USV: An experimental study. In Proceedings of the OCEANS 2019-Marseille, Marseille, France, 17–20 June 2019; pp. 1–5.
16. Kimball, P.W.; Clark, E.B.; Scully, M.; Richmond, K.; Flesher, C.; Lindzey, L.E.; Harman, J.; Huffstutler, K.; Lawrence, J.; Lelievre, S.; et al. The ARTEMIS under-ice AUV docking system. *J. Field Robot.* **2018**, *35*, 299–308. [CrossRef]
17. Wirtz, M.; Hildebrandt, M.; Gaudig, C. Design and test of a robust docking system for hovering AUVs. In Proceedings of the IEEE/MTS OCEANS, Hampton Roads, VA, USA, 14–19 October 2012; pp. 1–6.
18. Sarda, E.I.; Dhanak, M.R. Launch and recovery of an autonomous underwater vehicle from a station-keeping unmanned surface vehicle. *IEEE J. Ocean. Eng.* **2018**, *44*, 290–299. [CrossRef]
19. Piskura, J.C.; Purcell, M.; Stokey, R.; Austin, T.; Tebo, D.; Christensen, R.; Jaffre, F. Development of a robust Line Capture, Line Recovery (LCLR) technology for autonomous docking of AUVs. In Proceedings of the OCEANS 2016 MTS/IEEE Monterey, Monterey, CA, USA, 19–23 September 2016; pp. 1–5.
20. Sarda, E.I.; Dhanak, M.R. A USV-based automated launch and recovery system for AUVs. *IEEE J. Ocean. Eng.* **2016**, *42*, 37–55. [CrossRef]
21. Yang, C.; Peng, S.; Fan, S.; Zhang, S.; Wang, P.; Chen, Y. Study on docking guidance algorithm for hybrid underwater glider in currents. *Ocean Eng.* **2016**, *125*, 170–181. [CrossRef]
22. Palomeras, N.; Vallicrosa, G.; Mallios, A.; Bosch, J.; Vidal, E.; Hurtos, N.; Carreras, M.; Ridao, P. AUV homing and docking for remote operations. *Ocean Eng.* **2018**, *154*, 106–120. [CrossRef]
23. Fan, S.; Liu, C.; Li, B.; Xu, Y.; Xu, W. AUV docking based on USBL navigation and vision guidance. *J. Mar. Sci. Technol.* **2019**, *24*, 673–685. [CrossRef]
24. Feezor, M.D.; Sorrell, F.Y.; Blankinship, P.R.; Bellingham, J.G. Autonomous underwater vehicle homing/docking via electromagnetic guidance. *IEEE J. Ocean. Eng.* **2001**, *26*, 515–521. [CrossRef]
25. Peng, S.; Liu, J.; Wu, J.; Li, C.; Liu, B.; Cai, W.; Yu, H. A low-cost electromagnetic docking guidance system for micro autonomous underwater vehicles. *Sensors* **2019**, *19*, 682. [CrossRef] [PubMed]
26. Vandavasi, B.N.J.; Arunachalam, U.; Narayanaswamy, V.; Raju, R.; Vittal, D.P.; Muthiah, R.; Gidugu, A.R. Concept and testing of an electromagnetic homing guidance system for autonomous underwater vehicles. *Appl. Ocean Res.* **2018**, *73*, 149–159. [CrossRef]
27. Lin, R.; Zhao, Y.; Li, D.; Lin, M.; Yang, C. Underwater Electromagnetic Guidance Based on the Magnetic Dipole Model Applied in AUV Terminal Docking. *J. Mar. Sci. Eng.* **2022**, *10*, 995. [CrossRef]
28. Gutnik, Y.; Groper, M. Terminal Phase Navigation for AUV Docking: An Innovative Electromagnetic Approach. *J. Mar. Sci. Eng.* **2024**, *12*, 192. [CrossRef]
29. Zhong, L.; Li, D.; Lin, M.; Lin, R.; Yang, C. A fast binocular localisation method for AUV docking. *Sensors* **2019**, *19*, 1735. [CrossRef] [PubMed]
30. Singh, P.; Gregson, E.; Ross, J.; Seto, M.; Kaminski, C.; Hopkin, D. Vision-Based AUV Docking to an Underway Dock using Convolutional Neural Networks. In Proceedings of the 2020 IEEE/OES Autonomous Underwater Vehicles Symposium (AUV), St. Johns, NL, Canada, 30 September–2 October 2020; pp. 1–6.
31. Palomeras, N.; Penalver, A.; Massot-Campos, M.; Vallicrosa, G.; Negre, P.L.; Fernández, J.J.; Ridao, P.; Sanz, P.J.; Oliver-Codina, G.; Palomer, A. I-AUV docking and intervention in a subsea panel. In Proceedings of the 2014 IEEE/RSJ International Conference on Intelligent Robots and Systems, Chicago, IL, USA, 14–18 September 2014; pp. 2279–2285.
32. Hurtos, N.; Ribas, D.; Cufí, X.; Petillot, Y.; Salvi, J. Fourier-based registration for robust forward-looking sonar mosaicing in low-visibility underwater environments. *J. Field Robot.* **2015**, *32*, 123–151. [CrossRef]

33. Ferreira, F.; Djapic, V.; Micheli, M.; Caccia, M. Forward looking sonar mosaicing for mine countermeasures. *Annu. Rev. Control* **2015**, *40*, 212–226. [CrossRef]
34. Karimanzira, D.; Renkewitz, H.; Shea, D.; Albiez, J. Object detection in sonar images. *Electronics* **2020**, *9*, 1180. [CrossRef]
35. Wang, Z.; Guan, X.; Liu, C.; Yang, S.; Xiang, X.; Chen, H. Acoustic communication and imaging sonar guided AUV docking: System infrastructure, docking methodology and lake trials. *Control. Eng. Pract.* **2023**, *136*, 105529. [CrossRef]
36. Ferreira, F.; Machado, D.; Ferri, G.; Dugelay, S.; Potter, J. Underwater optical and acoustic imaging: A time for fusion? a brief overview of the state-of-the-art. In Proceedings of the OCEANS 2016 MTS/IEEE Monterey, Monterey, CA, USA, 19–23 September 2016; pp. 1–6.
37. Negahdaripour, S.; Taatian, A. 3-D motion and structure estimation for arbitrary scenes from 2 to D optical and sonar video. In Proceedings of the OCEANS 2008, Quebec City, QC, Canada, 15–18 September 2008; pp. 1–8.
38. Babaee, M.; Negahdaripour, S. 3-D object modeling from 2 to D occluding contour correspondences by opti-acoustic stereo imaging. *Comput. Vis. Image Underst.* **2015**, *132*, 56–74. [CrossRef]
39. Cardaillac, A.; Ludvigsen, M. Camera-Sonar Combination for Improved Underwater Localization and Mapping. *IEEE Access* **2023**, *11* , 123070–123079. [CrossRef]
40. International Submarine Engineering Ltd. Docking Systems. 2024. Available online : https://ise.bc.ca/product/dock/ (accessed on 21 December 2024).
41. Kalaitzakis, M.; Carroll, S.; Ambrosi, A.; Whitehead, C.; Vitzilaios, N. Experimental comparison of fiducial markers for pose estimation. In Proceedings of the 2020 International Conference on Unmanned Aircraft Systems (ICUAS), Athens, Greece, 1–4 September 2020; pp. 781–789.
42. Carreras, M.; Hernández, J.D.; Vidal, E.; Palomeras, N.; Ribas, D.; Ridao, P. SPARUS II AUV—A hovering vehicle for seabed inspection. *IEEE J. Ocean. Eng.* **2018**, *43*, 344–355. [CrossRef]
43. Quigley, M.; Conley, K.; Gerkey, B.; Faust, J.; Foote, T.; Leibs, J.; Wheeler, R.; Ng, A.Y. ROS: An open-source robot operating system. In Proceedings of the ICRA Workshop on Open Source Software, Kobe, Japan, 12–17 May 2009 ; Volume 3, p. 5.
44. Li, P.; Wang, H.; Yu, M.; Li, Y. Overview of image smoothing algorithms. *J. Phys. Conf. Ser. Iop Publ.* **2021**, *1883*, 012024. [CrossRef]
45. Murtagh, F.; Contreras, P. Algorithms for hierarchical clustering: An overview, II. *Wiley Interdiscip. Rev. Data Min. Knowl. Discov.* **2017**, *7*, e1219. [CrossRef]
46. Robotics, P. ArUco ROS Package. 2024. Available online: https://github.com/pal-robotics/aruco_ros (accessed on 1 April 2024 ).
47. Rosebrock, A. OpenCV Color Spaces (cv2. cvtColor). PyImageSearch. 2021. Available online: https://pyimagesearch.com/2021/04/28/opencv-color-spaces-cv2-cvtcolor/ (accessed on 20 May 2022).
48. Steger, C.; Ulrich, M.; Wiedemann, C. *Machine Vision Algorithms and Applications*; John Wiley & Sons: Hoboken, NJ, USA, 2018.
49. Yang, D.; He, B.; Zhu, M.; Liu, J. An extrinsic calibration method with closed-form solution for underwater opti-acoustic imaging system. *IEEE Trans. Instrum. Meas.* **2020**, *69*, 6828–6842. [CrossRef]
50. Raaj, Y.; John, A.; Jin, T. 3D Object Localization using Forward Looking Sonar (FLS) and Optical Camera via particle filter based calibration and fusion. In Proceedings of the OCEANS 2016 MTS/IEEE Monterey, Monterey, CA, USA, 19–23 September 2016; pp. 1–10.
51. Cieślak, P. Stonefish: An Advanced Open-Source Simulation Tool Designed for Marine Robotics, With a ROS Interface. In Proceedings of the OCEANS 2019—Marseille, Marseille, France, 17–20 June 2019. [CrossRef]